Generalized figure-control algorithm for large segmented telescope mirrors

Weiyao Zou

*Astronomical Optics Laboratory, National Astronomical Observatories, the Chinese
Academy of Sciences, and Nanjing Astronomical Instruments Research Center,
The Chinese Academy of Sciences, Nanjing 210042, China*

A fundamental discovery in segmented-mirror active optics is described: symmetrizing the geometry of the sensor–actuator array provides a computationally effective symmetrization of the mathematical description for the figure control of a Keck-type telescope mirror. The author establishes a universal mathematical control model and provides an efficient algorithm to solve this model equation set. This model can be applied to multifarious Keck-type mirror configurations with a similar sensor–actuator geometry design, no matter what kind of outline shapes and how many segments they have. With the underlying symmetry, a further extension of this algorithm is possible without increasing the number of parameters to be estimated for the recently proposed extremely large telescopes, such as the 30-m California Extremely Large Telescope (CELT) and the 100-m OverWhelmingly Large (OWL) telescope. Moreover, careful choice of boundary conditions in conjunction with the proper choice of minimization algorithm yields results that exceed the performance of the current existing techniques given by Nelson and Mast [Appl. Opt. **21**, 2631 (1982)]. This method allows noise performance analysis. Several computer simulation models for application of this algorithm are given for the Keck 10-m Telescope and the Large Sky Area Multi-Object Fiber Spectroscopic Telescope's (LAMOST's) M_A (Reflecting Schmidt plate) and M_B (spherical primary mirror).
    OCIS codes: 230.4040, 350.1260, 010.1080, 000.3860, 080.2720.

1. INTRODUCTION

In astronomy today, almost all the frontier explorations rely on the progress of new astronomical technologies. In order to upgrade angular resolution and detect more-remote nebulae, astronomical telescopes are being made with increasingly larger apertures. However, restricted by the gravity of our planet, our ability to improve the angular resolution by means of molding larger-aperture monolithic mirrors has reached its limit. It is very difficult to overcome the financial and technological difficulties associated with building a traditional telescope with larger than a 6-m aperture: the cost of building a traditional telescope is proportional to the third power of the telescope's aperture diameter.

Active Optics, born at the end of the 1970's, makes it possible for us to build even larger telescopes with lower cost and better optical quality. With this technique, the twin Keck 10-m telescopes, currently the largest optical telescopes in the world, were built. The primary mirror of this telescope is composed of 36 hexagonal mosaic segments. There are 168 capacitive displacement sensors installed underneath each intersegment edge for measuring the edge heights between segments, and three displacement actuators are installed on the back of each segment to provide three out-of-plane degrees of freedom. All 168 edge-height measurements together with three tilt measurements for the whole mirror configuration are used to compute the correction steps of 108 actuators (three of which are frozen to act as a fiducial segment). The optical figure of the primary mirror is controlled adaptively by moving actuators according to sensor readings.[1]

The central problem of active optics in a Keck-type telescope mirror is how to maintain the orientations and positions of the mirror segments to obtain the ideal mirror figure that we require. Translating the sensor information into the desired actuator motions is the task of a figure-control algorithm. This mathematical problem is closely related to the geometry of the sensor–actuator array, which determines the matrices of figure-control equations. Mast and Nelson proposed a figure-control design for Keck telescopes and analyzed it in detail in 1982.[1] The locations of the sensors and actuators of Keck telescopes are shown in Fig. 1.[2] A chi-square minimization technique is used to obtain the actuator motions for correcting the figure perturbations from the 171 readings of displacement sensors and tilt sensors.[1] To find the inverse matrix of the normal equation set, an efficient singular-value decomposition (SVD) algorithm is employed in their control system,[1] as described by Golub and Reinsch in 1970.[3] This inverse matrix is stored in a computer to eliminate repetitive computations.

With the success of Keck telescopes, telescope experts proposed more-ambitious configuration telescope projects, such as the 100-m OverWhelmingly Large (OWL),[4] the 30-m California Extremely Large Telescope (CELT),[5] and the Large Sky Area Multi-Object Fiber Spectroscopic Telescope (LAMOST).[6] To implement these designs we have to repeatedly study the figure-control algorithms for the diversified project configurations. Moreover, with the increase in the number of segments, providing the computing power needed for active optics control becomes a challenging problem. Thus we propose a question: can we find a generalized and efficient figure-control algo-
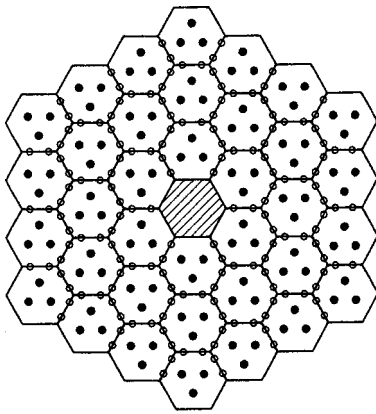
Fig. 1. Configuration of the primary mirror of the Keck 10-m telescope showing sensor and actuator locations.

rithm with which to solve all the figure-control problems of this sort?

In this paper we provide an answer to this question. We propose a generalized figure-control algorithm that fits all Keck-type segmented mirrors with multifarious boundary shapes and provides an efficient algorithm with which to obtain the actuator motions.

2. ESTABLISHMENT OF A FIGURE-CONTROL EQUATION SET FOR GENERAL PURPOSES

A. Mathematical Preparation
In plane analytic geometry, if the three vertices of a triangle counterclockwise are (x_1, y_1), (x_2, y_2), and (x_3, y_3), then the area of this triangle can be expressed as

$$S = \frac{1}{2}\begin{vmatrix} x_2 - x_1 & y_2 - y_1 \\ x_3 - x_1 & y_3 - y_1 \end{vmatrix}. \tag{2.1}$$

As shown in Fig. 2, the simplest configuration of a segmented mirror is that this mirror is composed of only two hexagonal segments. Although the segments are actually located on a large spherical surface (a hyperbolic surface for the Keck telescope), the sensor–actuator relations can be described in plane geometry with sufficient accuracy with respect to the relatively small curvature of the primary mirror.

In solid analytic geometry, a plane passing through three points counterclockwise, (x_1, y_1, z_1), (x_2, y_2, z_2), and (x_3, y_3, z_3), can be defined as

$$\begin{vmatrix} \mathbf{x} - x_1 & \mathbf{y} - y_1 & \mathbf{z} - z_1 \\ x_2 - x_1 & y_2 - y_1 & z_2 - z_1 \\ x_3 - x_1 & y_3 - y_1 & z_3 - z_1 \end{vmatrix} = 0. \tag{2.2}$$

Apparently, a sensor reading shows the height difference (the coordinate difference in the $\mathbf{z}$ axis) between the two adjacent segment planes at a boundary point. Assume that a sensor $\mathbf{s}$ is on the common boundary of segments M_1 and M_2 and that its coordinates are (ξ, η). Suppose that the initial heights of the three actuators of segment

M_1 are all zero and that after perturbation they become $\mathbf{z}_1$, $\mathbf{z}_2$, and $\mathbf{z}_3$. If the height of plane M_1 at (ξ, η) is $\mathbf{z}$, then

$$\mathbf{z} = \frac{\begin{vmatrix} \xi - x_1 & \eta - y_1 & \mathbf{z}_1 \\ \xi - x_2 & \eta - y_2 & \mathbf{z}_2 \\ \xi - x_3 & \eta - y_3 & \mathbf{z}_3 \end{vmatrix}}{\begin{vmatrix} x_2 - x_1 & y_2 - y_1 \\ x_3 - x_1 & y_3 - y_1 \end{vmatrix}}, \tag{2.3}$$

so $\mathbf{z}$ can be expressed as a linear polynomial of $\mathbf{z}_1$, $\mathbf{z}_2$, and $\mathbf{z}_3$, where $\xi - x_i$, $\eta - y_i$, $x_i - x_j$ and $y_i - y_j$ are constants. According to Eq. (2.1), we have

$$\mathbf{z} = \frac{1}{S_0}(S_1\mathbf{z}_1 + S_2\mathbf{z}_2 + S_3\mathbf{z}_3), \tag{2.4}$$

where S_0, S_1, S_2, and S_3 are the areas of $\Delta a_1 a_2 a_3$, $\Delta s a_2 a_3$, $\Delta s a_3 a_1$, and $\Delta s a_1 a_2$, respectively, and

$$S_1 + S_2 + S_3 = S_0. \tag{2.5}$$

Strictly, S_0, S_1, S_2, and S_3 should be the projected areas on the x–y plane. However, since the angle between the segment plane and the x–y plane is so small, the error that is introduced is negligible. From Eq. (2.4) we find that height $\mathbf{z}$ has no relation to the x–y coordinate system that we adopt but depends only on the sensor–actuator geometry. The value of $\mathbf{z}$ is a weighted sum of $\mathbf{z}_1$, $\mathbf{z}_2$, and $\mathbf{z}_3$, where the weighting coefficients are related only to the triangular areas among the actuators and the sensors.

Generally, the relative sensor–actuator geometry has two possible configurations, which are on the left and the right sides of Fig. 2. Suppose that the length of one side of each hexagonal segment is a, that the length of one side of the triangle formed by the three actuators under a segment is c, and that the distance between two sensors on a common boundary is d. Then the actuator triangle area in a segment is $S_0 = (\sqrt{3}/4)c^2$. When a sensor is on the same line as two actuators in a segment, the height motion of another actuator in the same segment does not contribute to this sensor reading. Therefore d should
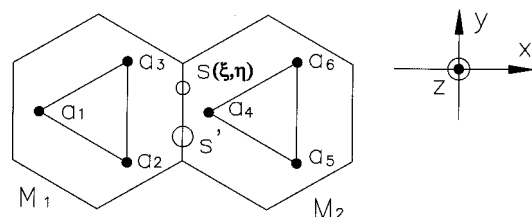

Fig. 2. Possible sensor–actuator geometrical relationships in two adjacent segments.

satisfy

$$\left| a - \frac{2}{3}c \right| \le d \le a + \frac{2}{3}c. \qquad (2.6)$$

Studying the two configurations of the sensor–actuator geometry yields the following results:

1.   On the left-hand side of Fig. 2, the heights of the left segment planes at the two sensor locations $\mathbf{s}$ and $\mathbf{s}'$ can be expressed as

$$\mathbf{z}_s = L_1\mathbf{z}_1 + L_2\mathbf{z}_2 + L_3\mathbf{z}_3,$$

$$\mathbf{z}_{s'} = L_1\mathbf{z}_1 + L_3\mathbf{z}_2 + L_2\mathbf{z}_3, \qquad (2.7)$$

where

$$L_1 = \frac{1}{3} - \frac{a}{c}, \qquad L_2 = \frac{1}{3} + \frac{a-d}{2c},$$

$$L_3 = \frac{1}{3} + \frac{a+d}{2c}.$$

Table 1.   Possible Geometrical Sensor–Actuator Position Permutations and the Corresponding Linear Coefficients in Eq. (2.9)

Type	Sensor-Actuator Geometries	C_1	C_2	C_3	C_4	C_5	C_6	Sensors
I		R_3	R_2	R_1	$-R_1$	$-R_2$	$-R_3$	$\mathbf{s}$
		R_2	R_3	R_1	$-R_1$	$-R_3$	$-R_2$	$\mathbf{s}'$
II		L_1	L_2	L_3	$-R_1$	$-R_2$	$-R_3$	$\mathbf{s}$
		L_1	L_3	L_2	$-R_1$	$-R_3$	$-R_2$	$\mathbf{s}'$
III		R_3	R_2	R_1	$-L_3$	$-L_2$	$-L_1$	$\mathbf{s}$
		R_2	R_3	R_1	$-L_2$	$-L_3$	$-L_1$	$\mathbf{s}'$
IV		L_1	L_2	L_3	$-L_3$	$-L_2$	$-L_1$	$\mathbf{s}$
		L_1	L_3	L_2	$-L_2$	$-L_3$	$-L_1$	$\mathbf{s}'$

2.   Similarly, for the right-hand side, the heights of the right segment planes at $\mathbf{s}$ and $\mathbf{s}'$ can be expressed as

$$\mathbf{z}_s = R_1\mathbf{z}_1 + R_2\mathbf{z}_2 + R_3\mathbf{z}_3,$$

$$\mathbf{z}_{s'} = R_1\mathbf{z}_1 + R_3\mathbf{z} + R_2\mathbf{z}_3, \qquad (2.8)$$

where

$$R_1 = \frac{1}{3} + \frac{a}{c}, \qquad R_2 = \frac{1}{3} - \frac{a+d}{2c},$$

$$R_3 = \frac{1}{3} - \frac{a-d}{2c}.$$

If we define a sensor reading as the difference in height of the adjacent segment planes at the sensor location, then the reading can be expressed as a linear representation of the six actuator lengths underneath the two segments. Therefore we have the following equation,

$$\mathbf{s} = C_1\mathbf{z}_1 + C_2\mathbf{z}_2 + C_3\mathbf{z}_3 + C_4\mathbf{z}_4 + C_5\mathbf{z}_5 + C_6\mathbf{z}_6, \quad (2.9)$$

and Table 1.   We find that if we know one sensor presentation (such as $\mathbf{s}$), then we can obtain another presentation ($\mathbf{s}'$) by swapping L_3 for L_2 and swapping R_3 for R_2. Therefore much repetition of deductions is avoided.

- • Actuator 1,2,...,147
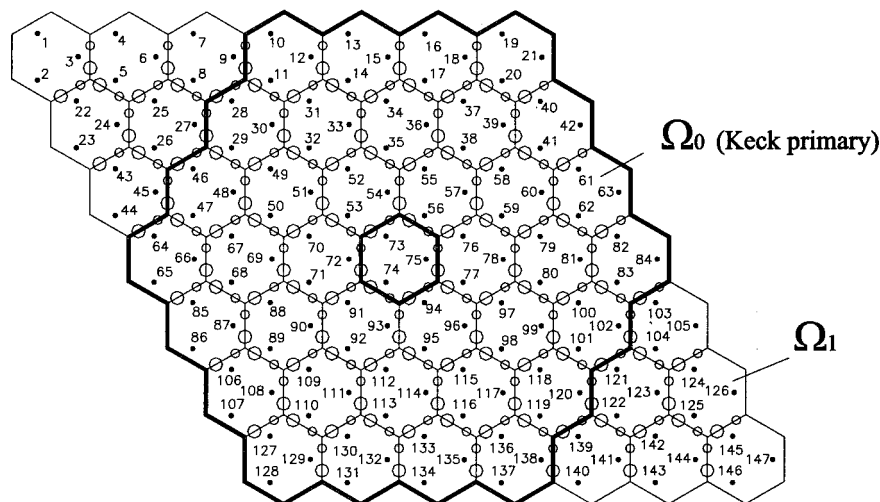- ○ Sensor 1,2,...,120
- ○ Sensor 1',2',...,120'

Fig. 3.   Universal schematic of a segmented mirror configuration for figure control.   The central hexagonal region is Ω_0, and the outer parallelogram region is Ω_1.   The actuator position distribution scheme is a proportional spacing array, which is different from that of the Keck 10-m telescope.

B. Establishment of a Generalized Equation Set for Segmented-Mirror Figure Control

The complexity of the coefficient matrix of a generalized figure-control equation set is closely related to the sensor–actuator position geometry and its serial numbering. For the Keck telescopes in Fig. 1 we can obtain 168 sensor–actuator relation equations similar to Eq. (2.9), which is an irregular large sparse linear equation set, and solving this equation requires a great deal of computation. Moreover, different primary configurations correspond to different coefficient matrices; therefore much repetitive research work has to be done when we encounter similar problems. In addition, it is difficult work to establish the giant equation set for an extremely large telescope such as the CELT and the OWL.

However, we discovered that if we adopt the actuator location design shown in Fig. 3, we can establish a large but regular sparse linear equation set and that a direct but efficient solving method can be employed to produce the solution. Therefore, as long as a segmented mirror can be encompassed by the parallelogram domain shown in Fig. 3, its figure-control equation set is obtained simultaneously, no matter what kinds of outline shapes and how many segments the mirror has.

Taking the Keck telescope primary mirror as an example, to make the coefficient matrix regular and simple we adopt the following regularizations for Fig. 3:

1. Add some imaginary segments to the configuration of the Keck primary and extend it to a parallelogram domain in which the actuator-position distribution geometry is a proportional spacing array and all the actuator position triangles in every segment have the same orientation.

2. Index the sensors (1–120 and $1'$–$120'$) and actuators (1–147) serially row by row (or, alternatively, column by column).

3. Let the additive virtual sensor readings be zero.

Suppose that the original sensor readings are zero and that after perturbations the sensor readings become s_i and s_i', $i = 1, 2 \ldots 120$; that the actuator motion lengths needed for correcting these sensor readings are p_i, $i = 1, 2 \ldots 147$; and that all the sensors have the same level measurement noise.

If $\mathbf{P} = (\mathbf{P}_1^T \ \mathbf{P}_2^T \ \mathbf{P}_3^T \ \mathbf{P}_4^T \ \mathbf{P}_5^T \ \mathbf{P}_6^T \ \mathbf{P}_7^T)^T = (p_1, p_2, \ldots, p_{147})^T$, then in Fig. 3, according to Type I in Table 1, we have

$$\begin{bmatrix} \mathbf{E} & & & \\ & \mathbf{E} & & \\ & & \ddots & \\ & & & \mathbf{E} \end{bmatrix} \begin{bmatrix} \mathbf{P}_1 \\ \mathbf{P}_2 \\ \vdots \\ \mathbf{P}_7 \end{bmatrix} = \begin{bmatrix} \mathbf{S}_1 \\ \mathbf{S}_2 \\ \vdots \\ \mathbf{S}_7 \end{bmatrix} \tag{2.10}$$

or

$$\mathbf{A}_1 \mathbf{P} = \mathbf{S}_\mathrm{I}, \tag{2.11}$$

where $\mathbf{S}_\mathrm{I} = (s_1 s_2 \ldots s_{42})^T$, and

$$\mathbf{E} = \begin{bmatrix} R_3 & R_2 & R_1 & -L_3 & -L_2 & -L_1 & & & & & & \\ & R_3 & R_2 & R_1 & -L_3 & -L_2 & -L_1 & & & & & \\ & & \ddots & \ddots & \ddots & \ddots & \ddots & \ddots & & & & \\ & & & & & R_3 & R_2 & R_1 & -L_3 & -L_2 & -L_1 \end{bmatrix}_{6 \times 21}. \tag{2.12}$$

According to Type II in Table 1, we have

$$\begin{bmatrix} \mathbf{B}_1 & \mathbf{C}_1 & & \\ & \mathbf{B}_1 & \mathbf{C}_1 & \\ & & \ddots & \ddots \\ & & & \mathbf{B}_1 & \mathbf{C}_1 \end{bmatrix} \begin{bmatrix} \mathbf{P}_1 \\ \mathbf{P}_2 \\ \vdots \\ \mathbf{P}_7 \end{bmatrix} = \begin{bmatrix} \mathbf{S}_8 \\ \mathbf{S}_9 \\ \vdots \\ \mathbf{S}_{13} \end{bmatrix} \tag{2.13}$$

or

$$\mathbf{A}_2 \mathbf{P} = \mathbf{S}_\mathrm{II}, \tag{2.14}$$

where $\mathbf{S}_\mathrm{II} = (s_{43}, s_{44}, \ldots, s_{84})^T$,

$$\mathbf{B}_1 = \begin{bmatrix} L_1 & L_2 & L_3 & & & & \\ & & L_1 & L_2 & L_3 & & \\ & & & \ddots & & & \\ & & & & L_1 & L_2 & L_3 \end{bmatrix}_{7 \times 21}, \tag{2.15}$$

$$\mathbf{C} = \begin{bmatrix} -R_1 & -R_2 & -R_3 & & & & \\ & & -R_1 & -R_2 & -R_3 & & \\ & & & \ddots & & & \\ & & & & -R_1 & -R_2 & -R_3 \end{bmatrix}_{7 \times 21}. \tag{2.16}$$

According to Type III in Table 1, again we have

$$\begin{bmatrix} \mathbf{B}_2 & \mathbf{C}_2 & & & \\ & \mathbf{B}_2 & \mathbf{C}_2 & & \\ & & \ddots & \ddots & \\ & & & \mathbf{B}_2 & \mathbf{C}_2 \end{bmatrix} \begin{bmatrix} \mathbf{P}_1 \\ \mathbf{P}_2 \\ \vdots \\ \mathbf{P}_7 \end{bmatrix} = \begin{bmatrix} \mathbf{S}_{14} \\ \mathbf{S}_{15} \\ \vdots \\ \mathbf{S}_{19} \end{bmatrix} \quad (2.17)$$

or

$$\mathbf{A}_3 \mathbf{P} = \mathbf{S}_{\mathrm{III}}, \quad (2.18)$$

where $\mathbf{S}_{\mathrm{III}} = (s_{85}, s_{86}, \ldots, s_{120})^T$,

$$\mathbf{B}_2 = \begin{bmatrix} 0 & 0 & 0 & R_2 & R_1 & R_3 & & & \\ & & & & R_2 & R_1 & R_3 & & \\ & & & & & \ddots & \ddots & \ddots & \\ & & & & & & R_2 & R_1 & R_3 \end{bmatrix}_{6\times21}, \quad (2.19)$$

$$\mathbf{C}_2 = \begin{bmatrix} -L_2 & -L_1 & -L_3 & & & & & & \\ & & & -L_2 & -L_1 & -L_3 & & & \\ & & & & & \ddots & \ddots & \ddots & \\ & & & & & & -L_2 & -L_1 & -L_3 & 0 & 0 & 0 \end{bmatrix}_{6\times21}. \quad (2.20)$$

Combining Eqs. (2.11), (2.14), and (2.18), we have

$$\begin{bmatrix} \mathbf{A}_1 \\ \mathbf{A}_2 \\ \mathbf{A}_3 \end{bmatrix} \mathbf{P} = \begin{bmatrix} \mathbf{S}_{\mathrm{I}} \\ \mathbf{S}_{\mathrm{II}} \\ \mathbf{S}_{\mathrm{III}} \end{bmatrix}, \quad (2.21)$$

which we rewrite as

$$\mathbf{A}_0 \mathbf{P} = \mathbf{S}_0. \quad (2.22)$$

We obtain $\mathbf{A}_0'$ by swapping L_3 for L_2 and swapping R_3 for R_2 in $\mathbf{A}_0$, and we obtain $\mathbf{S}_0'$ by replacing s_i with s_i' ($i = 1, 2, \ldots, 120$) in $\mathbf{S}_0$. Then we have

$$\mathbf{A}_0' \mathbf{P} = \mathbf{S}_0'. \quad (2.23)$$

Combining Eqs. (2.23) and (2.22), we have

$$\mathbf{A}\mathbf{P} = \mathbf{S}, \quad (2.24)$$

where

$$\mathbf{A} = \begin{bmatrix} \mathbf{A}_0 \\ \mathbf{A}_0' \end{bmatrix}_{240\times147}, \qquad \mathbf{S} = \begin{bmatrix} \mathbf{S}_0 \\ \mathbf{S}_0' \end{bmatrix}_{240\times1}.$$

Therefore the generalized figure-control equation set for the segmented mirrors is established. In this paper the generalized normal equation set is deduced for the case that each side of this extended segment array has seven segments (total 7×7 segments). However, our method is extensible to a general case of $n \times n$ segments, and the normal equation set needs only a few modifications.

To further economize the computation and memory space in solving the normal equations, the size of extended domain $\mathbf{\Omega}_1$ is selected adaptively to fit the segmented mirror $\mathbf{\Omega}_0$: If the segmented mirror is large, then the extended domain should be large; if the segmented mirror is small, then the extended domain should also be small. It is best that the size of $\mathbf{\Omega}_1$ be exactly big enough to accommodate the segmented mirror $\mathbf{\Omega}_0$. A larger extended domain is also workable, but it will waste some computation and memory space in solving the normal equations.

C. Deviation of the Normal Equation Set for Generalized Figure Control

Because of the redundancy of the sensor measurements, the least-squares (LS) technique is used to search for the solutions. So the normal equation set can be expressed as

$$\mathbf{A}^T \mathbf{A} \mathbf{P} = \mathbf{A}^T \mathbf{S}, \quad (2.25)$$

where

$$\mathbf{A}^T \mathbf{A} = \lfloor \mathbf{A}_0^T \mathbf{A}_0 + \mathbf{A}_0'^T \mathbf{A}_0' \rfloor_{147\times147}, \quad (2.26)$$

$$\mathbf{A}^T \mathbf{S} = \lfloor \mathbf{A}_0^T \mathbf{S}_0 + \mathbf{A}_0'^T \mathbf{S}_0' \rfloor_{147\times1}. \quad (2.27)$$

Deduction of $\mathbf{A}_0^T \mathbf{A}_0$ *and* $\mathbf{A}^T \mathbf{A}$

Let

$$\mathbf{R}_{(1)} = (R_3 \quad R_2 \quad R_1), \qquad \mathbf{L}_{(1)} = (-L_3 \quad -L_2 \quad -L_1), \quad (2.28)$$

$$\mathbf{R}_{(2)} = (-R_1 \quad -R_2 \quad -R_3), \qquad \mathbf{L}_{(2)} = (L_1 \quad L_2 \quad L_3), \quad (2.29)$$

$$\mathbf{R}_{(3)} = (R_2 \quad R_1 \quad R_3), \qquad \mathbf{L}_{(3)} = (-L_2 \quad -L_1 \quad -L_3), \quad (2.30)$$

and $\mathbf{O} = [0]_{3\times3}$. Then we obtain

$$\mathbf{A}_0^T \mathbf{A}_0 = \begin{bmatrix} \mathbf{D}_1 & \mathbf{F} & & & & \\ \mathbf{F}^T & \mathbf{D}_2 & \mathbf{F} & & & \\ & \ddots & \ddots & \ddots & & \\ & & \mathbf{F}^T & \mathbf{D}_2 & \mathbf{F} & \\ & & & & \mathbf{F}^T & \mathbf{D}_3 \end{bmatrix}_{147\times147}, \quad (2.31)$$

where

$$\mathbf{D}_1 = \begin{bmatrix} \mathbf{d}_1 & \mathbf{e} & & & \\ \mathbf{e}^T & \mathbf{d}_2 & \mathbf{e} & & \\ & \ddots & \ddots & \ddots & \\ & & \mathbf{e}^T & \mathbf{d}_2 & \mathbf{e} \\ & & & \mathbf{e}^T & \mathbf{d}_3 \end{bmatrix}_{21\times21}, \quad (2.32)$$

$$\mathbf{D}_2 = \begin{bmatrix} \mathbf{d}_4 & \mathbf{e} & & & \\ \mathbf{e}^T & \mathbf{d}_5 & \mathbf{e} & & \\ & \ddots & \ddots & \ddots & \\ & & \mathbf{e}^T & \mathbf{d}_5 & \mathbf{e} \\ & & & \mathbf{e}^T & \mathbf{d}_6 \end{bmatrix}_{21\times21}, \quad (2.33)$$

$$\mathbf{D}_3 = \begin{bmatrix} \mathbf{d}_7 & \mathbf{e} & & & \\ \mathbf{e}^T & \mathbf{d}_8 & \mathbf{e} & & \\ & \ddots & \ddots & \ddots & \\ & & \mathbf{e}^T & \mathbf{d}_8 & \mathbf{e} \\ & & & \mathbf{e}^T & \mathbf{d}_9 \end{bmatrix}_{21\times21}, \quad (2.34)$$

$$\mathbf{F} = \begin{bmatrix} \mathbf{f}_1 & & & \\ \mathbf{f}_2 & \mathbf{f}_1 & & \\ & \ddots & \ddots & \\ & & \mathbf{f}_2 & \mathbf{f}_1 \end{bmatrix}_{21\times21}, \quad (2.35)$$

where

$$\mathbf{d}_1 = \mathbf{L}_{(2)}^T \mathbf{L}_{(2)} + \mathbf{R}_{(1)}^T \mathbf{R}_{(1)}, \quad (2.36)$$

$$\mathbf{d}_2 = \mathbf{L}_{(1)}^T \mathbf{L}_{(1)} + \mathbf{L}_{(2)}^T \mathbf{L}_{(2)} + \mathbf{R}_{(1)}^T \mathbf{R}_{(1)} + \mathbf{R}_{(3)}^T \mathbf{R}_{(3)}, \quad (2.37)$$

$$\mathbf{d}_3 = \mathbf{L}_{(1)}^T \mathbf{L}_{(1)} + \mathbf{L}_{(2)}^T \mathbf{L}_{(2)} + \mathbf{R}_{(3)}^T \mathbf{R}_{(3)}, \quad (2.38)$$

$$\mathbf{d}_4 = \mathbf{L}_{(2)}^T \mathbf{L}_{(2)} + \mathbf{L}_{(3)}^T \mathbf{L}_{(3)} + \mathbf{R}_{(1)}^T \mathbf{R}_{(1)} + \mathbf{R}_{(2)}^T \mathbf{R}_{(2)}, \quad (2.39)$$

$$\mathbf{d}_5 = \mathbf{L}_{(1)}^T \mathbf{L}_{(1)} + \mathbf{L}_{(2)}^T \mathbf{L}_{(2)} + \mathbf{L}_{(3)}^T \mathbf{L}_{(3)} + \mathbf{R}_{(1)}^T \mathbf{R}_{(1)}$$
$$+ \mathbf{R}_{(2)}^T \mathbf{R}_{(2)} + \mathbf{R}_{(3)}^T \mathbf{R}_{(3)}, \quad (2.40)$$

$$\mathbf{d}_6 = \mathbf{L}_{(1)}^T \mathbf{L}_{(1)} + \mathbf{L}_{(2)}^T \mathbf{L}_{(2)} + \mathbf{R}_{(2)}^T \mathbf{R}_{(2)} + \mathbf{R}_{(3)}^T \mathbf{R}_{(3)}, \quad (2.41)$$

$$\mathbf{d}_7 = \mathbf{L}_{(3)}^T \mathbf{L}_{(3)} + \mathbf{R}_{(1)}^T \mathbf{R}_{(1)} + \mathbf{R}_{(2)}^T \mathbf{R}_{(2)}, \quad (2.42)$$

$$\mathbf{d}_8 = \mathbf{L}_{(1)}^T \mathbf{L}_{(1)} + \mathbf{L}_{(3)}^T \mathbf{L}_{(3)} + \mathbf{R}_{(1)}^T \mathbf{R}_{(1)} + \mathbf{R}_{(2)}^T \mathbf{R}_{(2)}, \quad (2.43)$$

$$\mathbf{d}_9 = \mathbf{L}_{(1)}^T \mathbf{L}_{(1)} + \mathbf{R}_{(2)}^T \mathbf{R}_{(2)}, \quad (2.44)$$

$$\mathbf{e} = \mathbf{R}_{(1)}^T \mathbf{L}_{(1)}, \quad (2.45)$$

$$\mathbf{f}_1 = \mathbf{L}_{(2)}^T \mathbf{R}_{(2)}, \quad (2.46)$$

$$\mathbf{f}_2 = \mathbf{R}_{(3)}^T \mathbf{L}_{(3)}. \quad (2.47)$$

Swapping L_3 for L_2 and swapping R_3 for R_2 in $\mathbf{A}_0^T \mathbf{A}_0$, we obtain $\mathbf{A}_0'^T \mathbf{A}_0'$. Then

$$\mathbf{A}^T \mathbf{A} = \mathbf{A}_0^T \mathbf{A}_0 + \mathbf{A}_0'^T \mathbf{A}_0'. \quad (2.48)$$

Deduction of $\mathbf{A}_0^T \mathbf{S}_0$ and $\mathbf{A}^T \mathbf{S}$
According to

$$\mathbf{A}_0^T \mathbf{S}_0 = \mathbf{A}_1^T \mathbf{S}_I + \mathbf{A}_2^T \mathbf{S}_{II} + \mathbf{A}_3^T \mathbf{S}_{III}, \quad (2.49)$$

we have

$$\mathbf{A}_0^T \mathbf{S}_0 = \begin{bmatrix} \mathbf{E}^T \mathbf{S}_1 + \mathbf{B}_1^T \mathbf{S}_8 + \mathbf{B}_2^T \mathbf{S}_{14} \\ \mathbf{E}^T \mathbf{S}_2 + \mathbf{B}_1^T \mathbf{S}_9 + \mathbf{C}_1^T \mathbf{S}_8 + \mathbf{B}_2^T \mathbf{S}_{15} + \mathbf{C}_2^T \mathbf{S}_{14} \\ \mathbf{E}^T \mathbf{S}_3 + \mathbf{B}_1^T \mathbf{S}_{10} + \mathbf{C}_1^T \mathbf{S}_9 + \mathbf{B}_2^T \mathbf{S}_{16} + \mathbf{C}_2^T \mathbf{S}_{15} \\ \mathbf{E}^T \mathbf{S}_4 + \mathbf{B}_1^T \mathbf{S}_{11} + \mathbf{C}_1^T \mathbf{S}_{10} + \mathbf{B}_2^T \mathbf{S}_{17} + \mathbf{C}_2^T \mathbf{S}_{16} \\ \mathbf{E}^T \mathbf{S}_5 + \mathbf{B}_1^T \mathbf{S}_{12} + \mathbf{C}_1^T \mathbf{S}_{11} + \mathbf{B}_2^T \mathbf{S}_{18} + \mathbf{C}_2^T \mathbf{S}_{17} \\ \mathbf{E}^T \mathbf{S}_6 + \mathbf{B}_1^T \mathbf{S}_{13} + \mathbf{C}_1^T \mathbf{S}_{12} + \mathbf{B}_2^T \mathbf{S}_{19} + \mathbf{C}_2^T \mathbf{S}_{18} \\ \mathbf{E}^T \mathbf{S}_7 + \mathbf{C}_1^T \mathbf{S}_{13} + \mathbf{C}_2^T \mathbf{S}_{19} \end{bmatrix}_{147\times1}.$$
$$(2.50)$$

A more-detailed expression of $\mathbf{A}_0^T \mathbf{S}_0$ is available. For example,

$$\mathbf{E}^T \mathbf{S}_2 + \mathbf{B}_1^T \mathbf{S}_9 + \mathbf{C}_1^T \mathbf{S}_8 + \mathbf{B}_2^T \mathbf{S}_{15} + \mathbf{C}_2^T \mathbf{S}_{14} = \begin{bmatrix} \mathbf{R}_{(1)}^T s_7 + \mathbf{R}_{(2)}^T s_{43} + \mathbf{L}_{(2)}^T s_{50} + \mathbf{L}_{(3)}^T s_{85} \\ \mathbf{L}_{(1)}^T s_7 + \mathbf{R}_{(1)}^T s_8 + \mathbf{R}_{(2)}^T s_{44} + \mathbf{L}_{(2)}^T s_{51} + \mathbf{L}_{(3)}^T s_{86} + \mathbf{R}_{(3)}^T s_{91} \\ \mathbf{L}_{(1)}^T s_8 + \mathbf{R}_{(1)}^T s_9 + \mathbf{R}_{(2)}^T s_{45} + \mathbf{L}_{(2)}^T s_{52} + \mathbf{L}_{(3)}^T s_{87} + \mathbf{R}_{(3)}^T s_{92} \\ \mathbf{L}_{(1)}^T s_9 + \mathbf{R}_{(1)}^T s_{10} + \mathbf{R}_{(2)}^T s_{46} + \mathbf{L}_{(2)}^T s_{53} + \mathbf{L}_{(3)}^T s_{88} + \mathbf{R}_{(3)}^T s_{93} \\ \mathbf{L}_{(1)}^T s_{10} + \mathbf{R}_{(1)}^T s_{11} + \mathbf{R}_{(2)}^T s_{47} + \mathbf{L}_{(2)}^T s_{54} + \mathbf{L}_{(3)}^T s_{89} + \mathbf{R}_{(3)}^T s_{94} \\ \mathbf{L}_{(1)}^T s_{11} + \mathbf{R}_{(1)}^T s_{12} + \mathbf{R}_{(2)}^T s_{48} + \mathbf{L}_{(2)}^T s_{55} + \mathbf{L}_{(3)}^T s_{90} + \mathbf{R}_{(3)}^T s_{95} \\ \mathbf{L}_1^{(T)} s_{12} + \mathbf{R}_{(2)}^T s_{49} + \mathbf{L}_{(2)}^T s_{56} + \mathbf{R}_{(3)}^T s_{96} \end{bmatrix}_{21\times1}. \quad (2.51)$$

The rest of the terms can be deduced by analogy.

In $\mathbf{A}_0^T \mathbf{S}_0$, replace s_i with s_i' ($i = 1, 2 \ldots 120$), swap R_3 for R_2, and swap L_3 for L_2, thus obtaining $\mathbf{A}_0'^T \mathbf{S}_0'$. Then we have

$$\mathbf{A}^T \mathbf{S} = \mathbf{A}_0^T \mathbf{S} + \mathbf{A}_0'^T \mathbf{S}_0'. \quad (2.52)$$

Two sides of the normal equations are obtained, and the normal equation set is established.

D. Solution Space of the Normal Equations

1. Compatibility of Domain Extension
Observing two sides of the normal equations, we find that on the right-hand side of a normal equation is the weighted sum of the sensor readings around a segment; and on the left side is the weighted sum of the actuators underneath this segment and its ambient segments. As for an interior segment, the sensor readings (displacement errors) around it are corrected together by 21 ambient segment actuator mo-

tions. This implies a smoothing effect for sensor noise in the meaning of LS in figure control.

Since the normal equation of a segment is related only to the ambient sensors and actuators, for the interior segments of Ω_0 the normal equations after domain extension remain the same as before, whereas for the boundary segments of Ω_0, which become the interior segments after domain extension, their corresponding normal equations have changed. However, we can demonstrate that these normal equations retain the boundary properties; at least these extended normal equations can be deduced to yield the same forms of expression as the previous boundary segments (or the corresponding boundary segments in Ω_1), under the condition that the additive sensor readings be zero. Therefore the regularizations that we made for the domain extension in Fig. 3 are reasonable, and the compatibility of this domain extension is just satisfied, at least approximately.

2. Droop Mode Control
It can be demonstrated that the rank of equation set (2.24) is $r(\mathbf{A}) = N - 4$, where N is the number of actuators. If all the sensor readings are zero and all the spherical segments have equal radii, the central normals to all the segments will cross at a point. This crossing point may move along the central normal to the fiducial segment within limits. Once the position of this point is determined, the figure of this segmented mirror is determined. The way in which to keep the correct position of this crossing point is a problem called droop mode control, whose effect on the optical image is simply a change of focus in some measure.[1]

Because of the overall telescope structure distortion that is due to temperature and gravity changes, the droop mode of the segmented mirror may drift slowly, whereas the sensor readings remain zero. Mast and Nelson once added three tilt sensors to monitor the whole figure of the primary mirror and keep the correct position of focus.[1] However, we found that if all the actuators are shaft encoded it is possible for us to maintain the droop mode without using the tilt sensors.

Suppose that $\mathbf{P}_0$ is the vector of the real-time readings of the actuator shaft encoders, $\Delta \mathbf{P}$ is the actuator motion vector, and $\Delta \mathbf{S} = \mathbf{S} - \mathbf{S}_{\text{phased}}$. We have

$$(\mathbf{A}^T \mathbf{A} + \boldsymbol{\delta}) \Delta \mathbf{P} = \mathbf{A}^T \Delta \mathbf{S} + \boldsymbol{\delta}(\mathbf{P}_{\text{phase}} - \mathbf{P}_0), \quad (2.53)$$

where $\mathbf{P}_{\text{phase}}$ can be the vector of the ideal readings of the actuator shaft encoders for the correct focal position or a vector for the primary tilt and piston, or a vector even for a conicoid surface as long as we require it; $\boldsymbol{\delta}$ is the damping diagonal matrix, and the elements of diagonal matrix $\boldsymbol{\delta}$ can be set specifically for controlling specific actuators. In this way, by assigning specific weights to the specific normal equations, we can control the primary mirror figure to an "arbitrary required shape."[7] In addition, we can use slope-measurement instruments, such as a Shack–Hartmann sensor, installed near the bent Cassegrain focus of the telescope to calibrate the droop mode and control it accordingly.

3. SOLUTION TO THE NORMAL EQUATIONS

A. Solving the Normal Equation Set by Employing the Cholesky Decomposition Method
When a mirror is composed of only a few segments, the search for a method of solving the normal equation set is not especially important, but when the number of segments increases, an efficient algorithm that requires less memory is necessary, because active optics needs real-time corrections. Mast and Nelson found their inverse matrix from the coefficient matrix of 105-sensor coupled linear equations, employing the SVD algorithm given by Golub and Reinsch.[3] To avoid repeated computation in real-time control, they store the inverse matrix in a computer and perform matrix multiplication with the sensor reading vector to obtain the actuator motions.[1]

Although the SVD algorithm is practicable for this generalized equation set, employing the Cholesky decomposition method in our problem will require less computation. We know that the normal equation set is always nonnegative definite, and it will be positive definite after addition of suitable constraints or a damping factor to the matrix. Therefore we can perform the Cholesky decomposition on it. The Cholesky method is a common direct method, and a similar application of it can be found in the literature.[8]

B. Memory Problem in Solving the Normal Equation Set
To solve the large sparse linear equation set, we must first clear up the coefficient matrix storage problem. We usually employ the compression storage method, eliminating the repeated zero elements in memory. Nevertheless, even if this method is used in our problem, to store the nonzero remainders and their pointers will still require too much space.

Fortunately, we find that the elements of the coefficient matrix can be expressed by a function $\mathbf{a}(i, j)$ whose values are zero and the corresponding elements of only 12 submatrices, $\mathbf{d}_1 \sim \mathbf{d}_9$, $\mathbf{e}$, $\mathbf{f}_1$, and $\mathbf{f}_2$ in Eqs. (2.32)–(2.35). Therefore only up to 108-element memory space is needed for storing this 147×49 matrix, even if the mirror configuration includes more segments. An additional 147×24 element memory space is required for the configuration in Fig. 3 to store a band matrix generated in Cholesky decomposition.

C. Solutions to the Figure-Control Problem

1. Least-Squares Solutions with Boundary Constraints
The rank of Eq. (2.25) is $N-4$, so if 4 of the 147 actuators are frozen, its solution will be unique. These 4 constraint points can be chosen arbitrarily in the parallelogram region shown in Fig. 3: real and virtual. Since the virtual segments can be regarded as the smooth extension of a real segmented mirror, if we constrain all the virtual actuator lengths to zero, the condition number of the normal equation set will be much improved and the corresponding solution will still satisfy our problem.

2. Least-Squares Solution with Minimum Norm
When three actuators are locked for a fiducial segment, the solution space has only one dimension; we need to de-

termine the droop mode. In mathematics, we can sort a LS solution that has minimum norm, so that the whole mirror will neither sag nor fold up.

Assume that this free actuator is $\mathbf{p}_1$; thus $\mathbf{p}_i$ can be expressed as the linear functions about $\mathbf{p}_1$. Let

$$\mathbf{\Psi} = \sum_{i=1}^{n} \mathbf{p}_i^2 = \sum_{i=1}^{n} (a_i \mathbf{p}_1 + b_i)^2. \qquad (3.1)$$

If $d\mathbf{\Psi}/dp_1 = 0$, we have

$$\mathbf{p}_1 = -\sum a_i b_i \bigg/ \sum_{i=1}^{n} a_i^2. \qquad (3.2)$$

According to Eqs. (3.1) and Eq. (3.2), we will obtain the LS solution with the minimum norm $\mathbf{p}_i$, $i = 1, \ldots, 147$.

3. Damped Least-Squares Solution

The solutions are the damped least-squares (DLS) solutions when the normal coefficient matrix is added with a damping diagonal matrix. The larger the damping factors are, the closer to zero the solutions are. It can be demonstrated that when the damping factor approaches zero, the DLS solution will tend toward the LS solution with minimum norm (MN).[7] The simulation computation demonstrates that when the damping factor is $\sim 10^{-6}$, there is almost no difference between the DLS solution and the LS solution with MN. In addition, it is also feasible to add constraints to the normal equation set in the DLS method.

4. ERROR PROPAGATION

The purpose of studying the error propagation is to explore the variation of the minimum point of the linear LS problem $\min_P \|\mathbf{S} - \mathbf{AP}\|$ with the perturbations of the coefficient matrix $\mathbf{A}^T \mathbf{A}$ and sensor readings $\mathbf{S}$.

Introduce norm $\| \cdot \|_2$

$$\|\mathbf{X}\|_2 = \sqrt{\mathbf{X}^T \mathbf{X}} = \left(\sum_{i=1}^{m} |x_i|^2 \right)^{1/2} \qquad (4.1)$$

and the corresponding matrix norm

$$\mathrm{lub}_2(\mathbf{A}) = \max_{x \neq 0} \sqrt{\frac{\mathbf{X}^T \mathbf{A}^T \mathbf{A} \mathbf{X}}{\mathbf{X}^T \mathbf{X}}} = \sqrt{\rho(\mathbf{A}^T \mathbf{A})} = \sqrt{\mathrm{lub}_2(\mathbf{A}^T \mathbf{A})}, \qquad (4.2)$$

where $\rho(\mathbf{A}^T \mathbf{A})$ is the spectral radius of $\mathbf{A}^T \mathbf{A}$. After perturbation, the normal equation becomes

$$(\mathbf{A} + \Delta\mathbf{A})^T (\mathbf{A} + \Delta\mathbf{A})(\mathbf{P} + \Delta\mathbf{P}) = (\mathbf{A} + \Delta\mathbf{A})^T (\mathbf{S} + \Delta\mathbf{S}). \qquad (4.3)$$

The perturbation of $\mathbf{A}$ is introduced by the size errors of the segments and the position errors of the actuators and sensors. If the position errors of the actuators and sensors are controlled within $\phi 5$ mm and we consider only the maximum positive errors, we obtain $\mathrm{lub}_2(\Delta\mathbf{A}) = 0.019$, which is so small that it can be ignored. Precisely, we can obtain the coefficient matrix by measuring
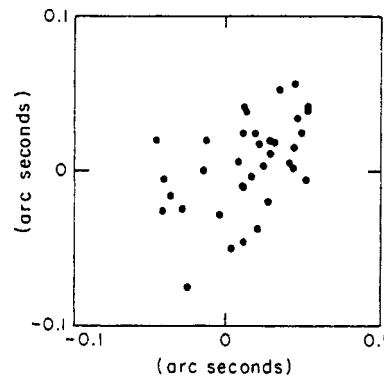

Fig. 4. Typical image spot diagram of the Keck 10-m primary mirror as given by Mast and Nelson,[1] which was generated by 50-nm rms displacement sensor noise.
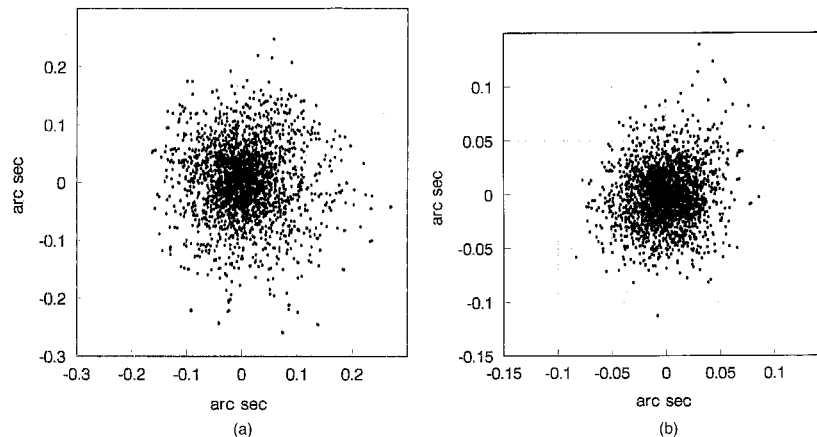

Fig. 5. (a) Superposition of 100 spot diagrams of the Keck primary mirror with four actuators locked: $p_{70} = p_{71} = p_{72} = p_{76} = 0$. The image's rms radius is 0.0794 arc sec. (b) Superposition of 100 spot diagrams of the Keck primary with all the virtual actuators constrained to zero. The image rms radius is 0.0277 arc sec.
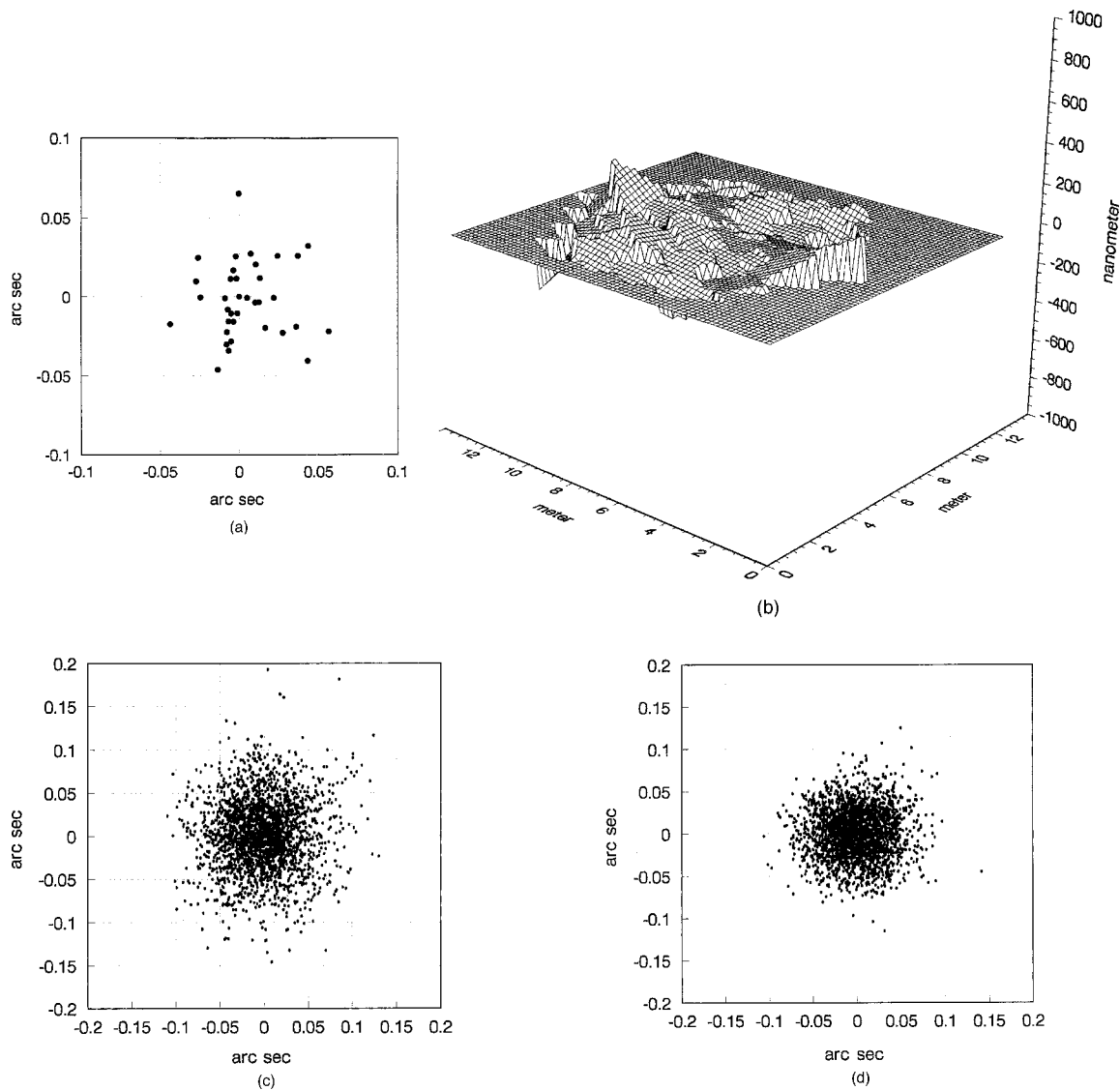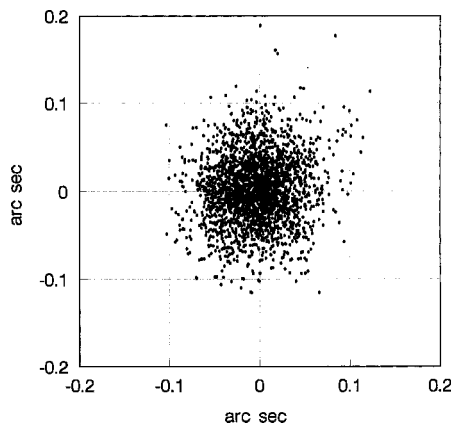
Fig. 6.   (a) Image spot diagram of the Keck primary mirror generated by the MN LS method with fiducial actuators $p_{70} = p_{71} = p_{72}$ = 0.0.   (b) Corresponding three-dimensional surface plot.   (c) Superposition of 100 image spot diagrams.   The image rms radius is 0.0499 arc sec, the 80% energy radius is 0.061 arcsec, and the rms surface error is 170.62 nm.   (d) Same as (c) but here the three fiducial actuators are $p_{19} = p_{65} = p_{138} = 0$.   The image rms radius is 0.04 arc sec and the rms surface error is 119.28 nm.

the influence function of the sensor–actuator system. Therefore, if we ignore the matrix perturbation, for the first-degree approximation we have[9]

$$\|\Delta \mathbf{P}\|_2 \leqslant \frac{[\,\text{cond}(\mathbf{A}^T\mathbf{A})\,]^{1/2}}{\text{lub}_2(\mathbf{A})} \|\Delta \mathbf{S}\|_2, \qquad (4.4)$$

where the condition number of $\mathbf{A}^T\mathbf{A}$ is defined as

$$\text{cond}(\mathbf{A}^T\mathbf{A}) = \text{lub}_2(\mathbf{A}^T\mathbf{A})\text{lub}_2\lfloor(\mathbf{A}^T\mathbf{A})^{-1}\rfloor. \qquad (4.5)$$

For the configuration shown in Fig. 3, $\text{lub}_2(\mathbf{A}) = 5.5$ and $\text{lub}_2(\mathbf{A}^T\mathbf{A}) = 30$.   The value of $\text{lub}_2\lfloor(\mathbf{A}^T\mathbf{A})^{-1}\rfloor$ changes greatly for different boundary conditions.   For example, in the case of a four-point constraint ($p_1 = p_2 = p_3$, p_4 = 10), $\text{lub}_2\lfloor(\mathbf{A}^T\mathbf{A})^{-1}\rfloor = 3 \times 10^{15}$; when all the virtual actuators are constrained to zero, $\text{lub}_2\lfloor(\mathbf{A}^T\mathbf{A})^{-1}\rfloor = 338$; when the damping factor is 1, $\text{lub}_2\lfloor(\mathbf{A}^T\mathbf{A})^{-1}\rfloor = 1.6$.   Obviously, the solution to the normal equations is sensitive to sensor noise in the case of a four-point constraint.

Notice that

$$\|\Delta \mathbf{S}\|_2 = \sqrt{n_s}\sigma_s, \qquad (4.6)$$

where n_s is the number of sensors, σ_s is the rms of sensor noise, and

$$\|\Delta \mathbf{P}\|_2 = \sqrt{n_p}\sigma_p, \qquad (4.7)$$

where n_p is the number of actuators and σ_p is the rms of actuator noise introduced by sensor noise.   We have

$$\sigma_p \leqslant \sqrt{\frac{n_s}{n_p}}\, \frac{[\,\text{cond}(\mathbf{A}^T\mathbf{A})\,]^{1/2}}{\text{lub}_2(\mathbf{A})}\,\sigma_s. \qquad (4.8)$$

This formula gives the estimation of the error propagation from sensors to actuators.

5. COMPUTER SIMULATIONS

To demonstrate the feasibility of the algorithm that we have proposed, we compose the simulation programs in C language and study the error propagation in this algorithm. For comparison of our results with those of Nelson and Mast,[1] all the sensor noise consists of the 50-nm rms Gaussian distribution random numbers generated by the C programs given in the literature.[10]

A. Simulation Computation of the Keck 10-m Segmented Mirror

The Keck telescope has 36 segments, 168 sensors, and 108 actuators. Figure 4 is a typical image spot diagram of a Keck 10-m primary mirror generated by 50-nm sensor noise as described by Nelson and Mast.[1] According to the superposition result of 100 spot diagrams,[1] the rms radius of the image distribution is $\sigma = 0.72\sigma_d$

Fig. 7.   Superposition of 100 image spot diagrams of the Keck primary mirror generated by the DLS method with three fiducial actuators $p_{70} = p_{71} = p_{72} = 0.0$. The damping factor is 10^{-6}. The image rms radius is 0.0482 arc sec.

$\times \sqrt{2} = 0.0509$ arc sec, and the image radius, which contains 80% of the energy, is $\mathbf{r}(80\%) = 1.8 \times 0.72\sigma_d = 0.062$ arc sec.

1. Result of the Constrained Least-Squares Method

Figure 5(a) is the simulation result for a four-point constraint. The image spot diagram is scattered, and it changes greatly when the constraint points are changed. However, the result will improve significantly if we constrain all the virtual actuators to zero, as shown in Fig. 5(b).

2. Least-Squares Method with Minimum Norm

Lock actuators p_{70}, p_{71}, and p_{72} to zero, and make use of actuator p_{76} as a free actuator (which one of these is chosen as the free actuator is not important): according to Eqs. (3.1) and (3.2) we will obtain the LS solution with MN. The simulation results are shown in Fig. 6. The image rms radius is 0.0499 arc sec, the image radius that contains 80% of the energy is 0.061 arc sec, and the rms surface error is 170.62 nm. This result agrees well with that of Mast and Nelson.[1] Moreover, we found that a better result [shown in Fig. 6(d)] will be obtained if we lock actuators p_{19}, p_{65}, and p_{138} to zero; the image rms radius is 0.04 arc sec.

3. Damped Least-Squares Method

The DLS method is also a good method for figure control of the segmented mirror in addition to its application in optical design.[11,12] The solution to the normal equation set is stable in this method. Compare Fig. 7 with Fig. 6(c); the DLS solution is only a little different from the MN LS solution when the damping factor is 10^{-6}.

- Actuator 1,2,...,147
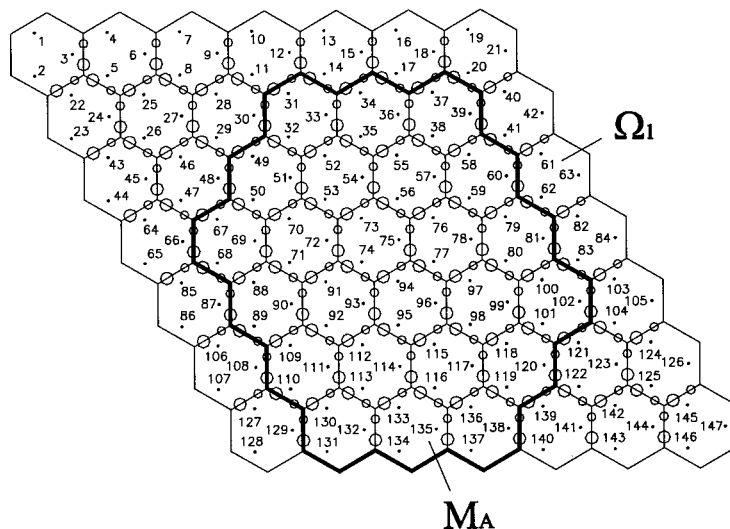
∘ Sensor 1,2,...,120

○ Sensor 1',2',...,120'

Fig. 8.   Configuration of M_A and its extended domain Ω_1 for the application of the generalized figure-control algorithm in the LAMOST.
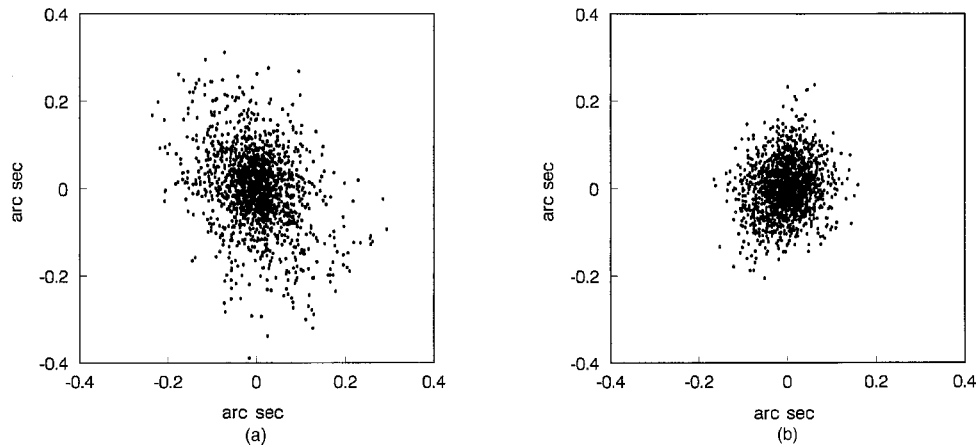
Fig. 9.   (a) Superposition of 100 image spot diagrams of the LAMOST mirror M_A generated by the LS method with four actuators locked: $p_{70} = p_{71} = p_{72} = p_{76} = 0.0$.   The rms surface error is 268.87 nm, the image rms rad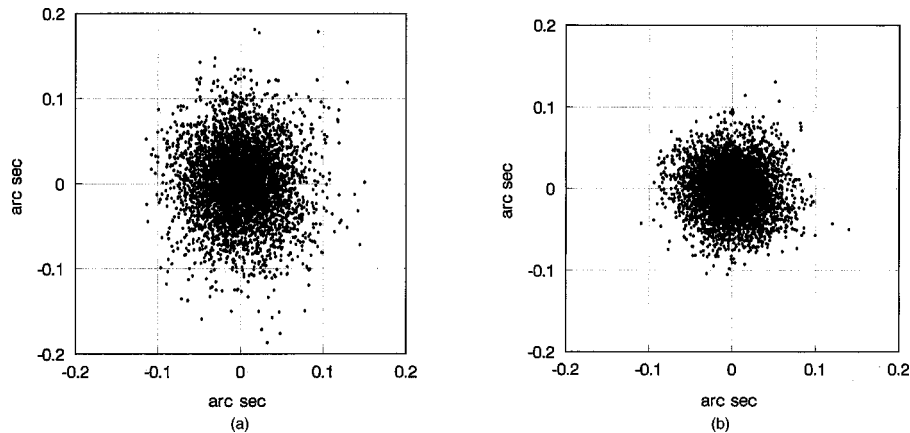ius is 0.107 arc sec, and the 80% energy radius is 0.126 arc sec.   (b) Superposition of 100 image spot diagrams of the LAMOST mirror M_A generated by the MN LS method with three fiducial actuators, $p_{70} = p_{71} = p_{72} = 0.0$.   The image rms radius is 0.074 arc sec and the 80% energy radius is 0.091 arc sec.

Fig. 10.   (a) Superposition of 200 image spot diagrams of the LAMOST mirror M_B generated by the MN LS method with three fiducial actuators, $p_{70} = p_{71} = p_{72} = 0.0$.   The image rms radius is 0.051 arc sec and the rms surface error is 183.14 nm.   (b) Same as (a) but with the three fiducial actuators replaced by $p_{19} = p_{65} = p_{138} = 0$.   The image rms radius is 0.0401 arc sec, and the rms surface error is 117.95 nm.

B.   Simulation Computation of the LAMOST

The LAMOST is a meridian reflecting Schmidt telescope with a 4-m clear aperture, a 20-m focal length, and a 5° field of view.   Employing the active optics technique to achieve its reflecting corrector (M_A) makes the LAMOST a unique astronomical instrument in combining a large aperture with a wide field of view.[6]   The aspheric mirror M_A is composed of 24 hexagonal segments, and spherical mirror M_B consists of 37 hexagonal segments.   Now we use the generalized figure-control algorithm to simulate the error propagation in M_A and M_B.

1.   Simulation Computation of M_A
There are 72 actuators and 110 displacement sensors in M_A.   The configuration of M_A and its extended domain Ω_1 are shown in Fig. 8, and the simulation results are shown in Fig. 9.   The image spot diagram in Fig. 9(a) is rather dispersed and has a ghostly outline shape of M_A.   Nevertheless, the result in Fig. 9(b) is much improved by

employing the MN LS method: The spot diagram becomes round and concentrated.

2.   Simulation Computation of M_B
Compared with the primary mirror of the Keck telescope (see Fig. 1), M_B has an additional central segment; therefore it has 180 sensors and 111 actuators.   Figure 10(a) shows a simulation result of M_B by the MN LS method, which is very close to the result for the Keck telescope shown in Fig. 6(c).   Figure 10(b) shows a better result that we obtained by changing the different actuators for the fiducial segment of M_B.

6. CONCLUSION

The generalized figure-control algorithm proposed in this paper provides a universal method for figure control of large segmented mirrors with irregular outlines. This study was performed during the first half of 1996 while

the author was working on his Master's thesis.[7] The conformance of the simulation results tothose of Mast and Nelson[1] demonstrates the feasibility of this generalized algorithm. By adoption of this symmetrical sensor–actuator geometry, this algorithm is extensible to the cases of the extremely large telescopes, such as 30-m CELT and the 100-m OWL.[4,5] In 1998 a successful application of this algorithm in the experimental system of segmented-mirror active optics in China[13] to control a ϕ500-mm mirror with three segments demonstrated the feasibility of this algorithm again. By employing this generalized figure-control algorithm we achieved a diffraction-limited image at a visible wavelength of $\lambda = 650$ nm over an aperture of ϕ220 mm in this experimental system. Because of the extreme regularity of the coefficient matrix that we built, the sophisticated SVD algorithm was replaced with a simpler and more efficient Cholesky decomposition algorithm for solving this normal equation set. We demonstrate that the LS solution with minimum norm can be obtained with enough precision by employing the damped LS method with very small damping factors[7]; therefore the computation in the figure-control algorithm is simplified, and the DLS algorithm is a good algorithm for figure control. To obtain a further stable solution, we can damp all the virtual actuators in the normal equations to zero to improve the stability of the coefficient matrix. A careful choice of the fiducial actuators in conjunction with a proper minimization algorithm makes it possible for us to further optimize the figure-control algorithm for segmented large telescopes.

ACKNOWLEDGMENTS

When this paper was submitted, W. Zou was a visiting scholar at Division of Geological and Planetary Sciences, California Institute of Technology, 150-21, Pasadena, California 91125. His present address is School of Optics/CREOL, P.O. Box 162700, University of Central Florida, Orlando, Florida 32816-2700. He can be reached by e-mail at zou@gps.caltech.edu and zou@odalab.ucf.edu.

1. T. S. Mast and J. E. Nelson, "Figure control for a fully segmented telescope mirror," Appl. Opt. **21**, 2631–2641 (1982).
2. R. C. Jared, A. A. Arthur, S. Andrede, A. Biocca, R. W. Cohen, J. M. Fuertes, J. Franck, G. Gabor, J. Llacer, T. Mast, J. Meng, T. Merrick, R. Minor, J. Nelson, M. Orayani, P. Salz, B. Schaefer, and C. Witebsky, "The W. M. Keck Telescope segmented primary mirror active control system," in *Advanced Technology Optical Telescope IV*, L. D. Barr, ed., Proc. SPIE **1236**, 996–1008 (1990).
3. G. H. Golub and C. Reinsch, "Singular value decomposition and least squares solutions," Numer. Math. **14**, 403–420 (1970).
4. R. Gilmozzi, B. Delabre, P. Diericky, N. Hubin, F. Koch, G. Monnet, M. Quatteri, F. Rigaut, and R. N. Wilson, "The future of filled aperture telescopes: is a 100 m feasible?" in *Advanced Technology Optical/IR Telescope VI*, L. M. Stepp, ed., Proc. SPIE **3352**, 778–791 (1998).
5. G. Chanan, J. Nelson, C. Ohara, and E. Sirko, "Design issues for the active control system of the California Extremely Large Telescope (CELT)," presented at the Astronomical Telescopes and Instrumentation 2000 meeting, Munich, Germany, March 27–31, 2000.
6. S. Wang, D. Su, Y. Chu, X. Cui, and Y. Wang, "Special configuration of a very large Schmidt telescope for extensive astronomical spectroscopic observation," Appl. Opt. **35**, 5155–5161 (1996).
7. W. Zou, "The figure control of large segmented mirror telescope," Master's thesis (Chinese Academy of Sciences, Nanjing, China, 1996).
8. W. Zou and Z. Zhang, "Generalized wave-front reconstruction algorithm applied in a Shack–Hartmann test," Appl. Opt. **39**, 250–268 (2000).
9. J. Stoer and R. Bulirsch, *Introduction to Numerical Analysis*, Chinese ed. (Springer-Verlag, New York, 1994).
10. W. H. Press, S. A. Teukolsky, W. T. Vetterling, and B. P. Flanery, *Numerical Recipes in C: The Art of Scientific Computing*, 2nd ed. (Cambridge U. Press, New York, 1998), pp. 278–283.
11. D. Su and Y. Wang, "Automatic correction of aberration in astro-optical system," Acta Astron. Sinica **15**, 51–60 (1974).
12. D. Su, "A merit function composed by spot-diagrams and the damp least square method," Opt. Instrum. Tech. No. 4, 1–12 (1980).
13. D. Su, W. Zou, Z. Zhang, Y. Qu, S. Yang, L. Wang, and Y. Rao, "Experiment system of segmented-mirror active optics," presented at the Astronomical Telescopes and Instrumentation 2000 meeting, Munich, Germany, March 27–31, 2000.